DE GRUYTER High Temperature Materials and Processes 2021; 40: 265–280

Research Article

Jyoti Menghani, Akash Vyas*, Satish More, Christ Paul, and Amar Patnaik

Parametric investigation and optimization for CO_2 laser cladding of AlFeCoCrNiCu powder on AISI 316

https://doi.org/10.1515/htmp-2020-0075
received January 11, 2020; accepted June 30, 2020

Abstract: The purpose of the current investigation is to analyze the effect of the operating parameters of laser-assisted cladding process on clad height, clad depth, clad width and the percentage dilution in a cladding of AlFeCuCrCoNi high-entropy powder on SS-316 through CO_2 laser and to optimize the cladding process parameters for optimum dilution. The experiments were designed by the full factorial method and analyzed by ANOVA. The analysis results indicate that dilution is most influenced by scanning speed followed by the powder feed rate. The outcomes of the single clad profile in terms of dilution, microhardness, composition and the microstructures produced in various cladding conditions are investigated briefly, and through which the optimum set of laser cladding operating parameters for maximum hardness of the clad material is determined. The optimum cladding conditions in the experimental range were obtained at 4 g/min powder feeding rate, 500 mm/min laser scanning speed and 1.1 kW laser beam power through multi-response optimization. Furthermore, the multi-track coating with 60% overlapping ratio was deposited using optimized parameters. The wear behavior of multi-track coating was determined using pin on disk wear apparatus with applied load of 20 N, sliding speed of 300 RPM and test duration of 15 min. The pin on disk wear test results indicates that the friction coefficient of SS-316 is larger than that of high-entropy alloy cladded SS-316. The wear resistivity of SS-316 improved by 40.35% after laser-assisted high-entropy alloy coating, which confirms that the laser cladding layer plays an essential role in enhancing the wear resistance capability of austenite steel.

Keywords: laser cladding, high-entropy alloy, microhardness, wear

1 Introduction

In the conventional method for alloying, the main concept involved mixing one or more elements with a majority of one element in a matrix, but the demand for alloys with extensive physical properties is increasing with time, and the traditional method of alloying is not adequate for the formation of new types of alloy. In 1990s, an innovative concept introduced by Yeh et al. has brought a revolution in the traditional alloy [1,2]. A solid solution alloys consisting of minimum five principal elements, but not more than 13 elements; each of the principal elements having a contribution of 5–35% in atomic fraction is designated as a multi-principal element alloy or high-entropy alloys (HEAs), and it is a hot frontline for the researchers in metallic material field [3]. The surface modification process in terms of coating consists of synthesizing a film of molten material onto a base material. The major purpose of cladding is to redefine the surface characteristic as an alternative to changing the composition of bulk material [4,5]. The HEA coating is produced with the help of several methods such as magneto sputtering, plasma transfer arc, electrochemical deposition and laser-assisted coating.

Laser cladding is an efficient surface cladding technique with an advantage of a rapid solidification rate (10^4–10^6°C/s), which eludes elemental segregation and enhancing solubility limitation. In addition, according to the kinetic theory, high solidification rate may lead to the reduction in the nucleation and growth rate of the brittle intermetallic compound [6,7]. There are three major operating factors such as scanning speed (mm/s), laser power (W)

---

* **Corresponding author: Akash Vyas,** Mechanical Engineering Department, SVNIT, Surat, Gujarat, India,
e-mail: akku.vyas2011@gmail.com
Jyoti Menghani: Mechanical Engineering Department, SVNIT, Surat, Gujarat, India
Satish More: V R Siddhartha Engineering College, Vijayawada, Andhra Pradesh, India
Christ Paul: Laser Additive Manufacturing Laboratory, RRCAT, Indore, Madhya Pradesh, India
Amar Patnaik: Mechanical Engineering Department, MNIT, Jaipur, Rajasthan, India

Table 1: Chemical Content of AISI 316

Element	C	Mg	Si	Cr	Ni	Mb	P	S	N_2	Fe
Wt%	0.08	2.00	0.1	16.0–18.0	10.0–14.0	2.00–3.00	0.045	0.03	0.1	65–70

Table 2: Percentage-wise composition of HEA powder

	Al	Fe	Cu	Co	Cr	Ni
Atomic no.	13	26	29	27	24	28
Wt%	8.85 ± 0.40	17.67 ± 0.10	19.71 ± 0.05	18.36 ± 0.20	16.32 ± 0.05	19.05 ± 0.25

and powder feed rate (mg/s). The other operating factors are laser spot size, speed of powder particle, flow rate, shielding gas, etc. [8,9]. However, their effect on the final properties of coating is less significant compared to the major operating parameters. Considering the several process parameters and their interdependencies, optimization of process parameters is still challenging.

Austenitic steel is extensively utilized in chemical industries, thermal as well as hydropower plant and marine environments attributable to their exceptional characteristics such as corrosion resistance, high strength and high durability. However, its capability to resist wear is comparatively low. Therefore, it is essential to enhance this property for application where wear occurs, such as nuclear power plants, hydropower plants and chemical industries by surface treatment [10,11,12].

The objective of the present work is to perform laser cladding experiments with HEA powder as a coating material and SS-316 as a base material to identify the effect of laser operating factors such as laser scanning speed and powder feed rate on clad height, clad width, clad depth and dilution percentage and to study the interdependency between coating morphology and its microhardness, wear resistivity along with X-ray diffraction (XRD) and energy dispersive spectroscopy (EDS) analyses.

2 Experimental procedure

2.1 Materials

The AISI 316 substrate was cut down from a long continuous rod of the metal to a circular shape, having 90 mm diameter and 10 mm thickness. An equiatomic Fe, Cr, Co, Ni, Cu and Al metal powders with an approximate size of around 100 μ were used as a cladding material. The chemical composition of the SS-316 and wt% contribution of individual elements of the cladding powder is mentioned in Tables 1 and 2, respectively. The reason behind selecting the particular individual element for making HEA is its mixing enthalpy with each other as listed in Table 3. The base material surface was polished with SiC paper (up to 1,200 grit size) and cleaned with the help of acetone prior to laser cladding.

2.2 Laser cladding

The quality as well as the performance of the coating layer is primarily influence by the operating factors of the laser cladding process, so it is essential to study the various parameters governing the cladding process [13]. Several researchers have deposited HEA coatings using laser cladding at different laser power. The optimum laser power mentioned was 1.0–1.1 kW. However, investigation with constant laser power and varying laser scanning velocity and cladding powder, the feed rate was relatively less [14–20]. Hence, in present the investigation, laser beam power remains unchanged and the remaining two crucial parameters were varied. The Fe, Cr, Co, Ni, Cu and Al metal powders with an approximate size of 100 μ were mixed in an equiatomic proportion using a 3D Multi-Motion Mixer (Alphie 0.3 HP) for 30 min (15 min forward and 15 min reverse cycle). The homogeneous mixture with purity of above 99.00% was fed to a 2 kW CO_2 laser rapid manufacturing (LRM) system situated in the Raja Rammna Center of Advance

Table 3: Binary mixing enthalpies, $\Delta H^{\text{mix}_{ij}}$ (kJ/mol) of high-entropy alloy [13]

	Al	Fe	Ni	Cu	Cr	Co
Al		−11	−22	−1	−10	−19
Fe	−11		2	13	−1	−1
Ni	−22	2		4	−7	0
Cu	−1	13	4		12	6
Cr	−10	−1	−7	12		−4
Co	−19	−1	0	6	−4	

Technology, Indore, Madhya Pradesh, India, as shown in Figure 1(a). The LRM system consists of a powerful laser system synchronized with the beam delivery system, powder feeding system and job manipulation system. Two coaxial feeders were engaged in the delivery of the metal powder mixture, keeping argon gas as a medium as well as shielding gas, as shown in Figure 1(b). The single track of the clad material with different process parameters, as shown in Table 4, was deposited on SS-316. The morphology of AlFeCoCuCrNi HEA coating synthesized over the SS-316 base material is shown in Figure 1(c and d).

2.3 Metallurgical and mechanical characterization

2.3.1 Clad profile measurement

The metallographic specimens were transverse cross-sectioned, Bakelite mounted, polished and etched with aqua regia. The clad dimensions, including clad height, clad width, molten depth and percentage dilution measured with the help of a vision measuring system (SDM-TRZ5 300; Spicon Instrument Industries, Ambala Cantt, Haryana, India) at 3× magnification. The equipment has a measuring range of 250 × 200 × 200 mm with resolution: 1 μm, repeatability ±2 μm, linear accuracy <5 μm and magnification up to 450×. Figure 2 shows the geometric aspects of a single track cross-section consisting of clad height, clad width, clad depth, clad area and diluted area. Another critical characteristic of clad

Table 4: Laser cladding operating factors

Operating factors	Level 1	Level 2	Level 3
Scanning velocity (mm/min)	300	400	500
Powder feed rate (g/min)	2	3	4
Laser power (kW)	1.1		
Spot diameter (mm)	2.4		
Argon flow rate (LPM)	6		
Standoff distance (mm)	8		

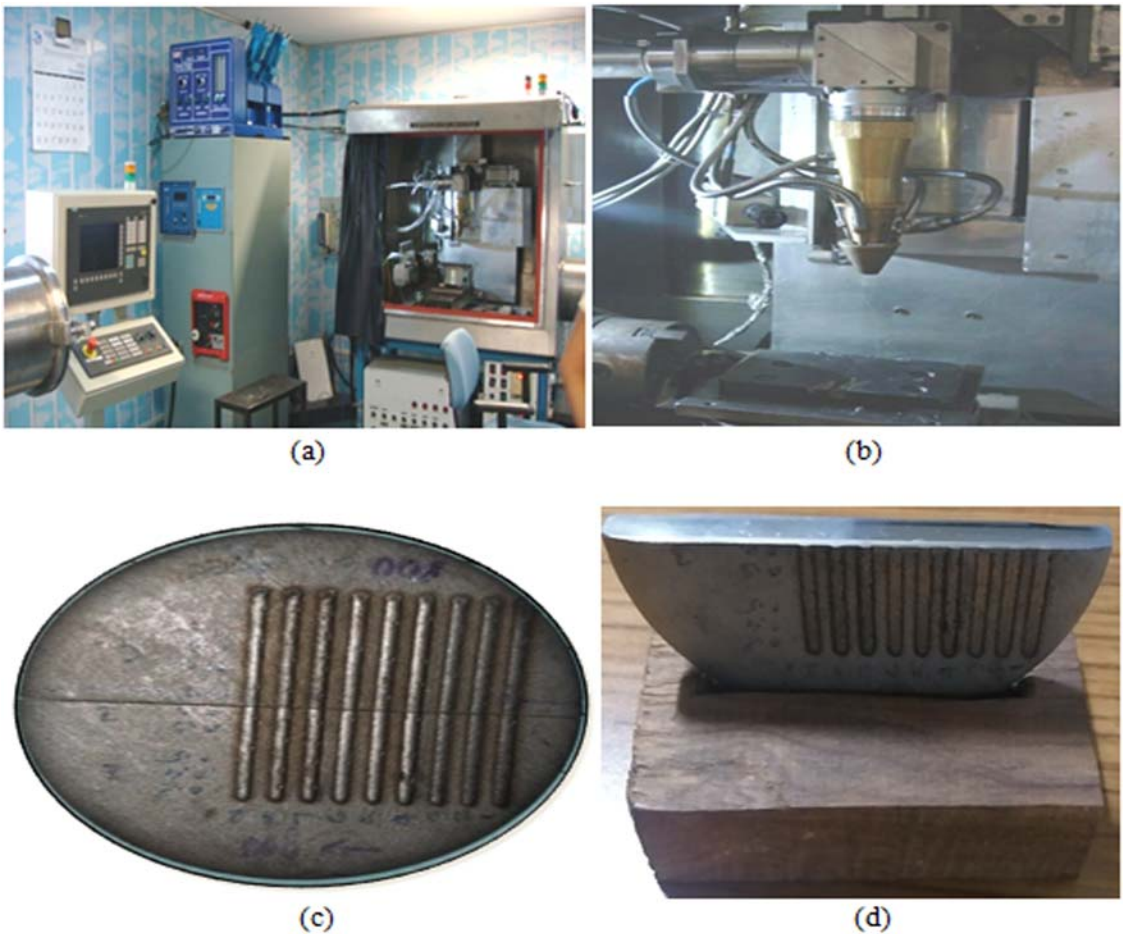
(a) (b) (c) (d)

Figure 1: (a) Laser cladding experimental setup, (b) laser head, (c) single clad structure and (d) cross-sectional view for microscopic observation.

structure is called dilution, and it can be derived by equation (1) [9,11,17].

$$\text{Dilution (\%)} = \frac{A_d}{A_c + A_d} \tag{1}$$

2.3.2 Metallurgical observation

The difference in the clad morphology throughout its length and height was revealed with the aid of an optical microscopy. The microstructure of the AlFeCuCoCrNi HEA coating was analyzed using an optical microscope (Leica S8APO) at 100×, 200× and 400× magnification. The phases of coatings were identified with the help of an XRD using a RIGAKU diffractometer with Cu-Kα radiation, and origin 8.0 software used to analyze the data. The Energy dispersive spectrometer analyzed the elemental distribution in the coating as well as in the interface zone (JSM-7100F).

2.3.3 Microhardness measurement

The microhardness of the coating layers, initiating from the cladding surface to the base material, was determined with the help of micro Vickers' hardness tester (FM 700; Future Tech Corporation, Japan) by applying a load of 0.5 kg with a dwell time of 15 s. The displacement between the two consecutive points of indentation was 0.1 mm.

2.3.4 Wear testing

The tribological performance of the cladding was investigated with the aid of pin on disc wear apparatus (DUCOM-TR-20LE) in unlubricated condition and at room temperature. The testing was conducted in accordance with the procedure given in ASTM standard G-99. The EN31 with a size of ϕ 120 × 10 mm and the hardness of HRC 61-65 was used as a counterpart. The specimen with dimension 10 mm × 10 mm × 10 mm was polished with 1,200 grit abrasive paper before wear test. The final magnitudes for mass loss during wear test were taken from the average of the three experimental runs. The wear specimens were worn for 15 min under a load of 20 N and a sliding speed of 300 RPM. The microstructure of the worn surface was also characterized by the S3400N SEM. The coefficient of friction was estimated with the help of equation (2):

$$\text{Friction coefficient } (\mu) = \frac{M}{RP} \tag{2}$$

where M = friction moment, R = counterpart radius, P = normal load acting on the target material [11].

The wear resistance of the specimen was estimated through the method of weight loss. Before and after the experimental runs, the samples were cleaned with acetone and the mass loss was determined by an analytical balance (AnaMatrix-AMX4D) with the least count of 0.1 mg.

3 Results and discussion

3.1 Geometrical measurement

To form a desirable clad profile along with clad quality, the proper selection of integrated factors is to be made. Figure 3 indicates the metallographic sectional assessment of the single-clad structure using vision measuring system at different powder feed rates and scanning

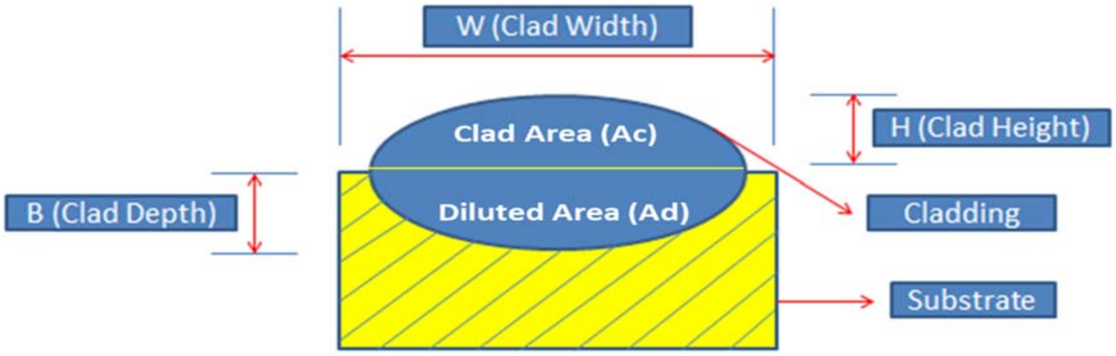

Figure 2: Dimensional characteristics of melt pool profile.

speed. The qualitative significance of the major operating factors on the dimensional characteristic of a single clad structure can be revealed from Figure 3. At the first glimpse, well-fused single-clad structures were observed by combining all the operating parameter combinations.

For the parametric study, the full factorial method was used with three levels of powder feed rates and laser scanning speed, while the other parameters such as laser power (1,100 W), argon flow rate (6 LPM), spot diameter (2.4 mm) and standoff distance (8 mm) remained invariable. The experimental results in terms of clad height, clad width, molten depth and the percentage dilution are indicated in Table 5.

3.2 Clad height

The clad height is one of the crucial geometrical aspects of the clad structure. The clad height falls off with a rise in the scanning speed, as shown in Figure 4. The reason behind this phenomenon is an increment in the scanning speed that leads to a decrease in interaction time. Hence, the volume of the molten cladding material deposited in the melt pool reduces. Besides the laser scanning speed, the powder feed rate also plays a vital role in determining the clad height [14,15]. As shown in Figure 4, increment in powder feed rate leads to a rise in clad height. However, increasing the powder feed rate leads to an increase in the powder quantity per unit area, so the clad height increases [11]. From the above discussion, it was found that we can achieve a maximum clad height (0.308 mm) with the maximum scanning velocity of 500 mm/min and a maximum powder flow rate of 4 g/min.

3.3 Clad width

As shown in Figure 5, the width of the cladding is more or less equivalent to beam diameter and declines linearly with a rise in the laser scanning speed at a constant cladding powder feed rate. The reason behind this linear relation is the availability of less heat through the laser beam at the base material surface, as the laser power available per unit length decreases with an increase in the scanning speed. The powder feed rate has a negative impact on clad width. The decrement in powder feed rate led to a reduction in clad width as lesser amount of laser power is required to melt the coating material. From the

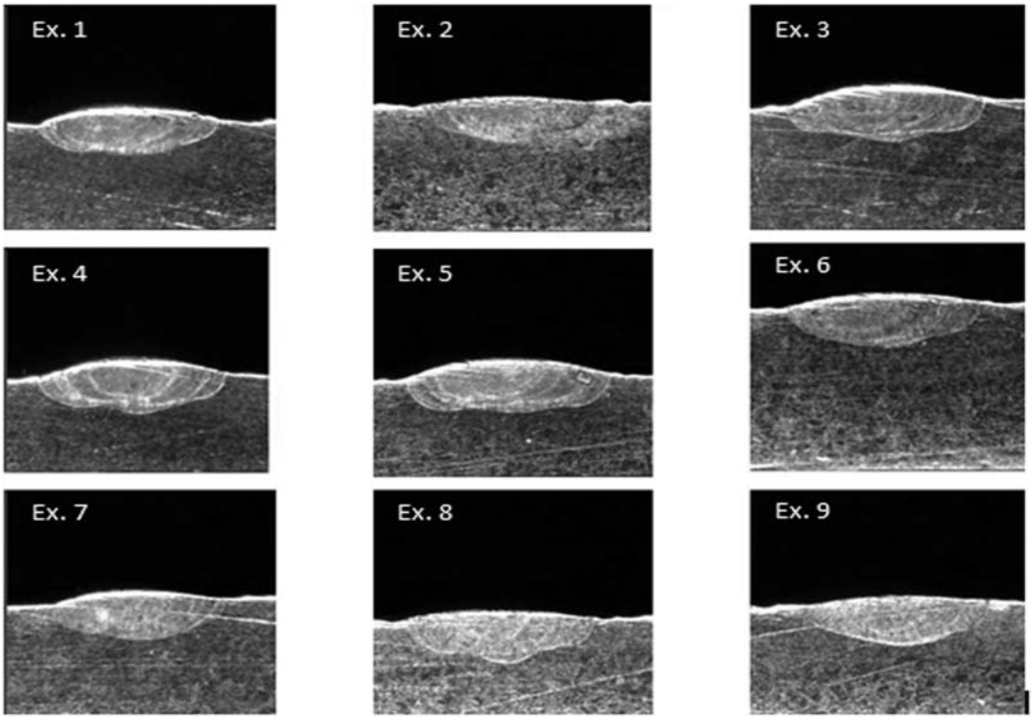

Figure 3: Morphology of single clad structure.

Table 5: Experimental results

S. no.	Scanning speed (mm/min)	Powder feed rate (g/min)	Clad height (mm)	Clad width (mm)	Clad depth (mm)	Clad area (mm^2)	Diluted area (mm^2)	Dilution (%)
1	300	3	0.185	2.291	0.376	0.212	0.430	67.0
2	400	3	0.223	2.21	0.376	0.246	0.415	62.7
3	500	4	0.308	2.163	0.283	0.333	0.306	47.8
4	500	2	0.223	2.098	0.3	0.234	0.314	57.3
5	400	4	0.228	2.232	0.297	0.254	0.331	56.5
6	300	2	0.147	2.265	0.373	0.166	0.422	71.7
7	300	4	0.192	2.298	0.338	0.221	0.388	63.7
8	500	3	0.25	2.16	0.327	0.270	0.353	56.6
9	400	2	0.222	2.125	0.376	0.233	0.395	62.8

above discussion, it was found that we can achieve the maximum width (2.298 mm) with a minimum laser scanning velocity of 300 mm/min and a maximum powder feed rate of 4 g/min.

3.4 Clad depth

In the laser cladding process, the laser energy is divided into three parts: absorption by substrate, absorption by powder and refection by powder and base material. The laser energy that reached to the base material is the power residue after depletion by powder cloud either by absorption or by reflection. The energy depleted by powder is directly proportional to the metal powder feed rate [14]. Hence, with increasing powder feed rate, a larger portion of the laser energy will be absorbed by the powder rather than the base material, leading to a reduction in penetration into the substrate. On the other hand, increasing the laser scanning speed can decrease the heat generated per unit area at a time, and then less laser power is consumed by the base material in the equivalent time, causing a reduction in clad depth. It can also be confirmed by Figure 6. From the above discussion, it was found that we can achieve minimum clad depth (0.283 mm) with a maximum laser scanning speed of 500 mm/min and maximum powder feed rate of 4 g/min.

3.5 % Dilution

The laser scanning speed as well as powder feed rate inversely affects the dilution of the clad material. That consequence was due to the following reasons. Higher scanning speed can decrease the heat input rate and then less laser energy is absorbed by the base material at the same period, resulting in a decreased percentage of dilution. The increment in powder feed rate creates more powder material that covers the surface of the base material, and less laser energy is injected onto the base material, similar to that with scanning speed [16]. It can also be justified as shown in Figure 7. To investigate the

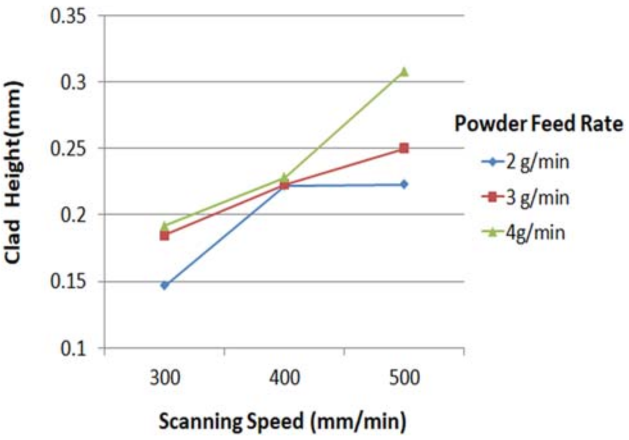

Figure 4: Effect of process parameter for clad height.

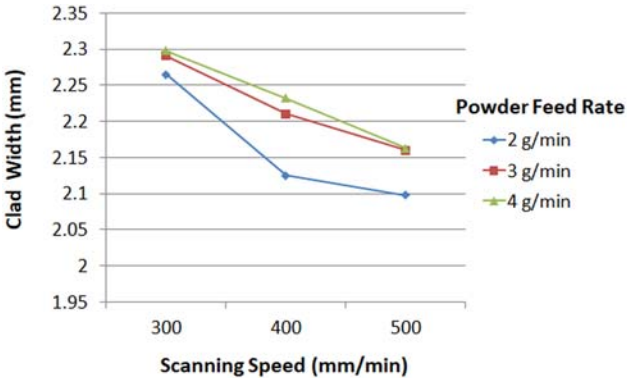

Figure 5: Effect of process parameter for clad width.

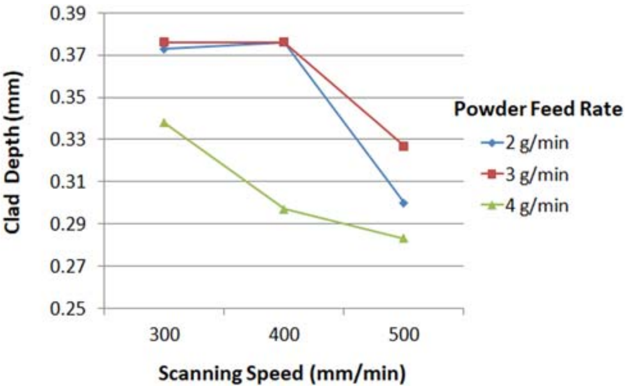

Figure 6: Effect of process parameter for clad depth.

effects of operating parameters cumulatively, two factors were determined, namely, mass feed rate and linear energy input, which can be defined by the following formula:

$$\text{Mass feed rate (g/mm)} = \frac{\text{Powder feed rate (g/min)}}{\text{Cladding speed (mm/min)}} \tag{3}$$

The mass feed rate (g/mm) parameter was well defined so as to summarize the effect of powder feed rate (g/min) and cladding or scanning speed (mm/min) on clad structure and quality. The linear energy input (J/mm) factor was well defined so as to summarize the effect of laser beam power (W) and cladding speed (mm/min) on the clad structure and quality [10].

$$\text{Linear energy input (J/mm)} = \frac{\text{Laser beam power (W)}}{\text{Cladding speed (mm/min)}} \tag{4}$$

To evaluate the effects of the linear energy input (J/mm) and mass feed rate (g/mm) on the dilution, a contour graph was generated (Figure 8). As shown in Figure 8, the maximum dilution (71.7%) was achieved with a linear energy input of 220 J/mm and a mass feed rate of 0.006 g/mm. This result reveals that the linear energy input has a direct influence on the dilution and can be considered as a leading factor in the contour plot division area (Figure 8). The minimum dilution (47.8%) occurred when the linear energy input was 132 J/mm and the mass feed rate was 0.008 g/mm. Therefore, the result reveals that increment in the mass feed rate resists the base material from excessive melting and, therefore, lower level of dilution can be obtained [10].

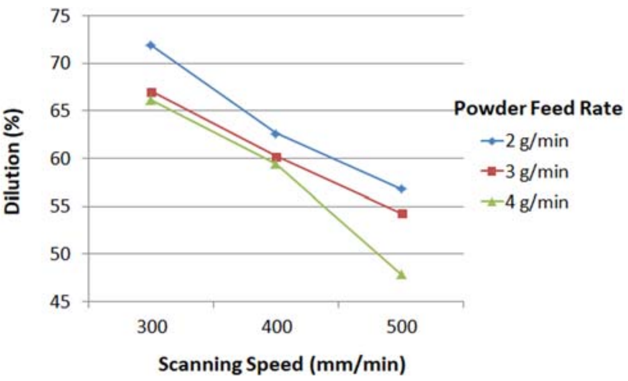

Figure 7: Effect of process parameter for dilution.

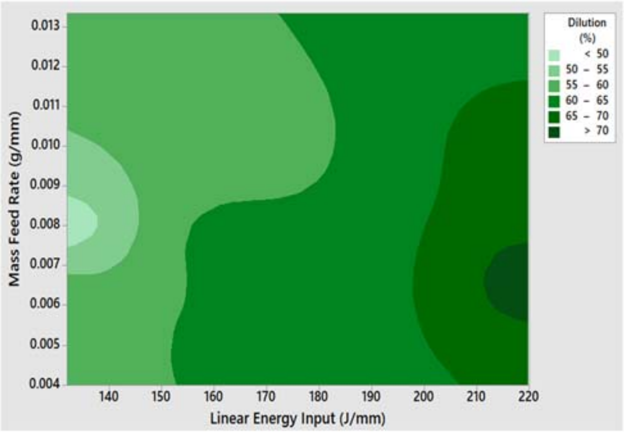

Figure 8: Contour plot for dilution.

3.6 ANOVA analysis

ANOVA is a statistical technique that is used to investigate and model the relationship between a response variable and one or more independent variables. Each explanatory variable (factor) consists of two or more categories (levels). ANOVA tests the null hypothesis that the population means of each level are equal versus the alternative hypothesis that at least one of the level means are not all equal. ANOVA helps to investigate whether the process parameters are significant or not and the effect of parameters on performance characteristics. ANOVA identifies the significance of parameters on responses. ANOVA table states the different values such as square of means, degree of freedom, sum of square (SS), *F* value and *P* value. The significance of factor depends on the *P* value which supposes to be less than 0.05. The basic ANOVA terminology is listed as follows:

- SS: it is the square of the deviation from the grand mean of the response.

$$\text{Adj. mean square (MS)} = \frac{\text{Adj. sum of square}}{\text{Degree of freedom}} \tag{5}$$

- *F* value: it is used to check the adequacy of the model by the given formula,

$$F\text{-value} = \frac{\text{Adj. mean of square}}{\text{Error means square}} \tag{6}$$

- P value: it provides a way of testing the relationship between independent variable and the response.
- R^2 (coefficient of determination): which measures the amount of reduction in variability of the response or R^2 indicates how well the model fits your data.
- R^2 (adj.): adjusted R^2 is a modified R^2 that has been adjusted for the number of terms in the model.
- R^2 (Pred.): used in regression analysis to indicate how well the model predicts responses for new observations. Predicted R^2 can prevent overfitting the model.

As seen from the ANOVA in Table 6, the laser scanning velocity and powder feed rate both are the most influencing factor for percentage dilution. From the main effect plot, it was observed that percentage dilution is minimum at a scanning speed of 500 mm/min and powder feed rate of 4 g/min. The above result follows the fundamental of dilution. Normal probability plot indicates that points follow the straight line, so residuals are normally distributed and the fit is good enough. ANOVA results for percentage dilution indicate dilution is significantly influenced by scanning speed with a contribution of 70.70% and P = 0.001, followed by powder feed rate with a contribution of 26.48% and P = 0.009. The model is sufficiently accurate at R^2 97.18% and R^2 (adj) 94.35%.

3.7 Multi-response optimization

The multiple response optimization is predicated on the desirability function approach. The optimization module searches for an amalgamation that concurrently satiates the desirable placed on each of the responses and factors in an endeavor to obtain the apt model. The objective of the optimization processes is to identify the optimum magnitude of input parameters in laser-assisted coating process to achieve better quality and geometry of the clad structure. To deal with this type of contradictory objective problem, the desirability function approach is used [17].

$$\text{DF} = \left(\prod_{i=1}^{n} d_i^{wi}\right)^{1/\sum_{j-1}^{n} wi} \tag{7}$$

$$F(x) = -\text{DF} \tag{8}$$

If the aim is to obtain a particular magnitude of T_i, the desirability d_i can be express as,

Table 6: ANOVA table for % dilution

Source	DF	Seq. SS	Contribution (%)	Adj. SS	Adj. MS	F value	P value
Scanning speed	2	274.85	70.70	274.85	137.423	50.05	0.001
Powder feed rate	2	102.93	26.48	102.93	51.465	18.74	0.009
Error	4	10.98	2.82	10.98	2.746		
Total	8	388.76	100.00				

Model summary	S	R^2	R^2 (adj.)	Press
	1.65698	97.18%	94.35%	55.5980

$$d_i = 0 \text{ if } \leq \min_i \tag{9}$$

$$d_i = \left[\frac{Y_i - \min_i}{T_i - \min_i}\right] \quad \text{if } \min_i \leq Y_i \leq T_i \tag{10}$$

$$d_i = \left[\frac{Y_i - \max_i}{T_i - \max_i}\right] \quad \text{if } T_i \leq Y_i \leq \min_i \tag{11}$$

$$d_i = 0 \quad \text{if } Y_i \geq \max_i \tag{12}$$

where di = desirability for the ith response, w_i = weighting of desirability, Y_i = Value of the ith output, $\min_i$ = minimum value of the ith response, $\max_i$ = maximum value of the ith response, T_i = target value of the ith response.

For multi-response optimization target, upper and lower limit of response, the parameters are predefined as shown in Table 7. The optimum operating parameter combinations for maximum cladding height, maximum cladding width, minimum penetration depth and minimum dilution were 4 g/min powder feed rate and 500 mm/min scanning velocity as indicated in Figure 9.

3.8 Microhardness

Microhardness measurements were carried out at three regions including cladding zone, interface zone and substrate zone across the HEA cladded SS-316. The enhancement of microhardness in the cladding zone is due to solid solution strengthening initiated from a considerable variation in the atomic radius of the alloying individual elements. The variation in atomic radius leads to lattice distortion and results in considerable residual compressive stress in cladding [14,18]. The hardness value decreases in the following sequence: clad zone, interface zone or dilution zone and substrate region. The hardness fluctuation within the clad zone depends on processing conditions. However, due to the crystal phase, with the increase in laser scanning speed, the grain is refined, and the hardness of the crystal phase is enhanced [19,20]. Therefore, the coating has the peak hardness at laser scanning velocity of 500 mm/min.

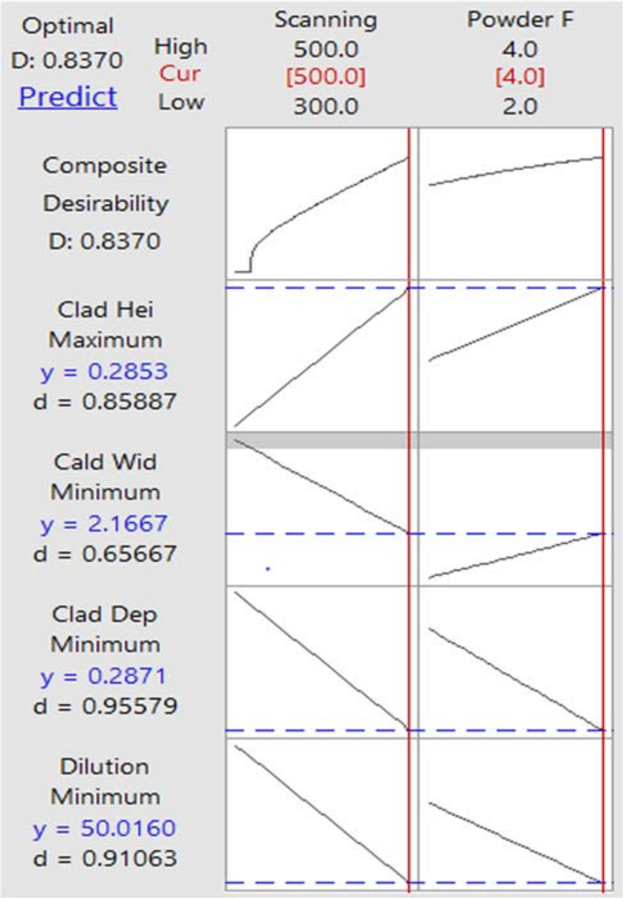

Figure 9: Optimization plot for clad geometry.

As shown in Figure 10, the microhardness values enhance with decreasing percentage dilution. The maximum microhardness (241 HV) was achieved at minimum percentage dilution (47.8%) and clad parameters at 500 mm/min scanning speed and 4 g/min powder feed rate; while at 300 mm/min laser scanning velocity and 2 g/min cladding powder feed rate, the average hardness was 180 HV due to maximum dilution of 71.7%. The decreasing microhardness is due to the influence of substrate property in the cladding structure.

Table 7: Identification for lower and upper limit of responses for optimization

Response	Goal	Lower	Target	Upper	Weight	Importance
Clad height	Maximize	0.147	0.308	0.308	1	1
Clad width	Maximize	2.098	2.298	2.298	1	1
Clad depth	Minimize	0.283	0.283	0.376	1	1
Dilution (%)	Minimize	47.8	47.8	71.7	1	1

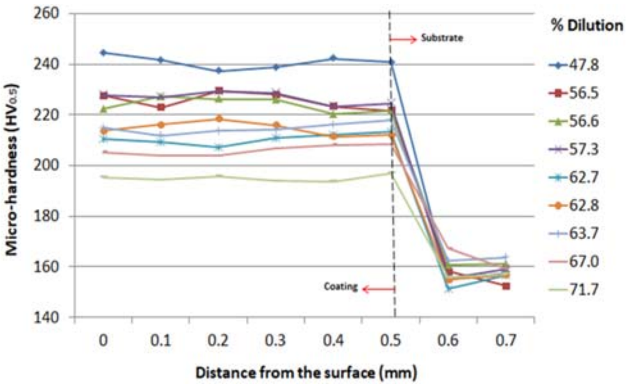

Figure 10: Microhardness with respect to the percentage dilution for single clad structures.

3.9 Constituent phases

The XRD analysis for sample having maximum and minimum microhardness value among the nine clad structure is given in Figure 11(a). While Figure 11(b) indicates the XRD of HEA powder and HEA-coated multi-track (with optimum process parameters) substrate. The XRD analysis of the powder was done after mixing the powder properly through a multi-motion mixer. The graph clearly suggests the presence of each element that was incorporated and homogenously distributed. The phases formed in coatings depend on the (1) melting point temperature, (2) composition and (3) solidification rate. For AlFeCoCuCrNi HEA, its mixing entropy reached a peak with an equiatomic ratio. Hence, it forms a solid solution, rather than intermetallic or ordered phases. On the other hand, Boltzmann's hypothesis suggested that the high mixing entropy of solid solutions along with multiple principle elements reduces the tendency to segregation and ordering. The multi-track coating with 60% overlapping ratio was analyzed after cooling down, and it was found that the formation of both structures body centered cubic (BCC) and face centered cubic (FCC) but there is no sign of intermetallic.

According to the Hume–Rothery rule, factors such as ΔH, ΔS, ΔX and valence electron concentration (VEC) can play an essential role in the formation of solid solution. Several researchers concluded that when the magnitude of δ (atomic size difference) in between 1% and 6%, ΔH_{mix} (mixing enthalpy) is in between −15 and 7 kJ/mol, ΔS_{mix} (mixing entropy) in between 11 and 19.5 J/K mol, Ω more than and equal to 1.1, VEC less than and equal to 8.0 and ΔX (electronegativity difference) leads to form solid solution. In the present investigation, the values obtained are shown in Table 8, indicating the formation of stable solid solution [21–27]. Furthermore, XRD spectra did not show any oxide in the laser-assisted cladding, indicating that adequate protection against oxidation was obtained during laser cladding. The XRD peak intensities indicate that the volume fraction of FCC is considerably more than BCC. The presence of BCC structure is due to the atom-level strain effect of Al in AlCoCrCuFeNi. The presence of Al element with a higher atomic radius leads to a higher elastic strain and a higher atomic packing efficiency (APE) in laser cladded HEA coatings. The dissolution of Al can also be observed, which further combines to form BCC crystalline phase [21–23]. Per the XRD graph, increase in percentage dilution percentage leads to give an additional peak in terms of iron. Both of the XRD have a combination of FCC + BCC phases but as the percentage dilution increases (microhardness decreases) and additional peaks of iron were observed. The reduction in microhardness is due to the influence of iron contribution to degrade the coating properties in terms of microhardness.

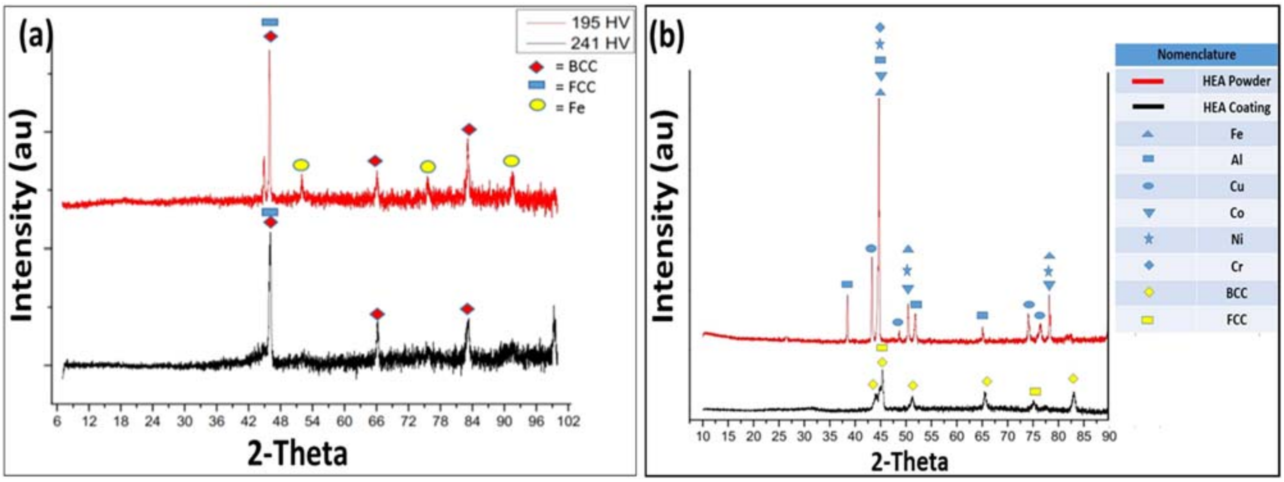

Figure 11: XRD of (a) minimum and maximum hardness value of single clad and (b) HEA powder and coating.

Table 8: Parameters of AlCrFeNiCuCo HEA coating [27]

Alloys	δ (%)	ΔS_{mix} (J/K mol)	ΔH_{mix} (kJ/mol)	T_m (K)	Ω	VEC	ΔX
AlCrFeNiCuCo	4.82	14.9	−4.78	1622.25	5.06	7.83	0.109

3.10 Optical microstructure and EDS observations

Optimized process parameters consist of the following parameter set: laser beam power of 1.1 kW, cladding powder feed rate of 4 g/min and laser scanning velocity of 500 mm/min for minimum dilution (47.8%). Figures 12 and 13 is a micrograph of a single laser track transverse cross section with maximum and minimum dilution, respectively. Figures 12 and 13(a) show the microscopic features of the minimum and maximum dilution specimen and Figures 12 and 13(b) shows the cladding zone, while Figures 12 and 13(c) shows an interface zone. The clad coating with minimum dilution (47.8%) is free from pores and cracks, while coating with maximum dilution (71.7%) consists of some interface cracks and pores. The fine cracks at interface for maximum dilution sample were attributed to the high temperature gradient between the cladding layer and the substrate due to the low powder feed rate and slow scanning speed. The quick directional solidification can be observed at the interface zone of the cladding where the growth direction of the columnar grains is perpendicular to the interface line. It is caused by the high temperature gradient in laser-assisted cladding process. The columnar grains transform to equiaxed grains with reducing temperature gradient in the center of the coatings. Figures 12 and 13(c) show the details of the microstructure along the interface line of the laser cladded SS-316. The interface line indicates a curved shape, instead of a straight line, indicating that the cladding layer and the base material have a good metallurgical bond, which plays a vital role in the performance of the material [28]. Close examination revealed a change in the mode of solidification from primary ferrite, as seen commonly, to primary austenite. The presence of intercellular or interdendritic ferrite is further evidence of such a change in the mode of solidification. This may be rationalized due to the excessive undercooling at the tip of the primary delta-ferrite cells or dendrites that could have changed the mode of solidification from primary delta-ferrite to primary austenite [29].

The EDS results for the elemental composition of multi-track HEA cladded specimen in regions A (clad zone), B (near to interface zone) and C (interface zone) is shown in Figure 14. The outcomes reveal that all the elements (Al, Co, Cu, Cr and Ni) are evenly distributed through the clad zone, near to the interface zone and in an interface zone excluding iron. There is approximately 3 wt% increment in iron percentage in the interface zone as compared to the clad zone. The increment in iron percentage is due to the influence of substrate material composition (consists 65%–70 wt% of iron). The EDS results reveal that the iron content is more than the theoretical content in the clad zone, near to the interface zone as well as in the interface zone due to the quick heating rate of the high-energy laser beam. During laser cladding, the substrate material melts along with the cladding powder, which leads to increased iron content as we move toward the interface zone. The small thin layer of substrate SS-316 melt and then solidification together with the cladding material, iron content was increased, but marginally shows appropriate dilution during processing [29].

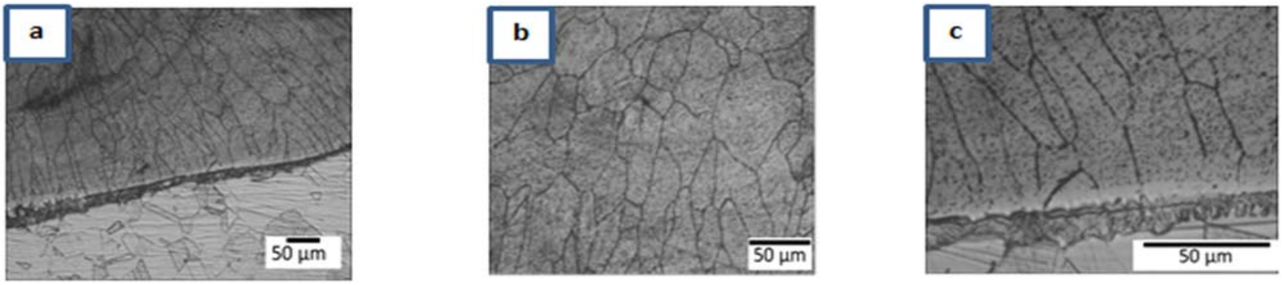

Figure 12: Cross-sectional microstructure of single clad structure with maximum dilution (a) interface zone with lower magnification, (b) cladding zone with higher magnification and (c) interface zone with higher magnification.

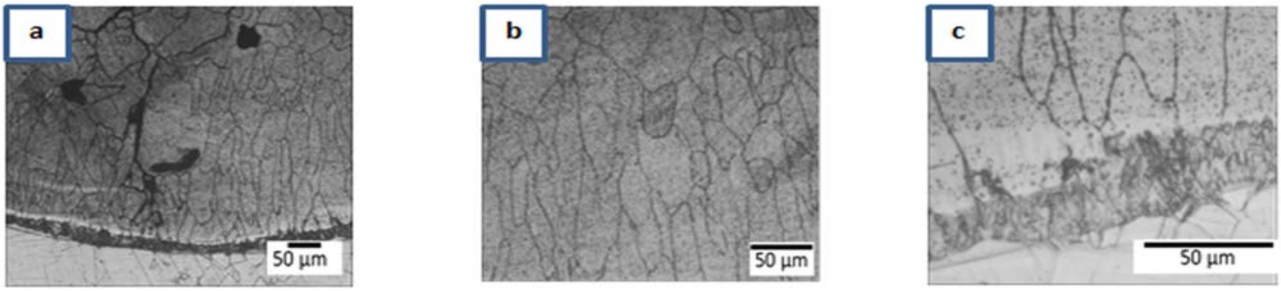

Figure 13: Cross-sectional microstructure of single clad structure with maximum dilution (a) interface zone with lower magnification, (b) cladding zone with higher magnification and (c) interface zone with higher magnification.

3.11 Friction and wear behavior

The tribological performance of HEA was assessed by a pin on disc wear test apparatus. The samples utilized for friction and wear tests were made by multi-pass laser cladding (60% overlapping ratio) with the optimum operating factors obtained from the laser-assisted cladding process (laser power: 1.1 kW, powder feed rate: 4 g/min, scanning speed: 500 mm/min, argon flow rate: 6 LPM, spot diameter: 2.4 mm and standoff distance: 8 mm). The graph of friction coefficient with respect to time for cladded as well as untreated sample is shown in Figure 15. The friction coefficient graph is typically characterized by two friction regimes as reported in the literature [1,7]. Initially, the coefficient of friction increases rapidly until reaching a peak value μ_p. Then a gradual decrease is followed to a steady-state value μ_{ss}. Their ranges of friction coefficient are different, as listed in Table 9. Both the friction curvatures of a specimen with and without laser cladding show a peak coefficient of

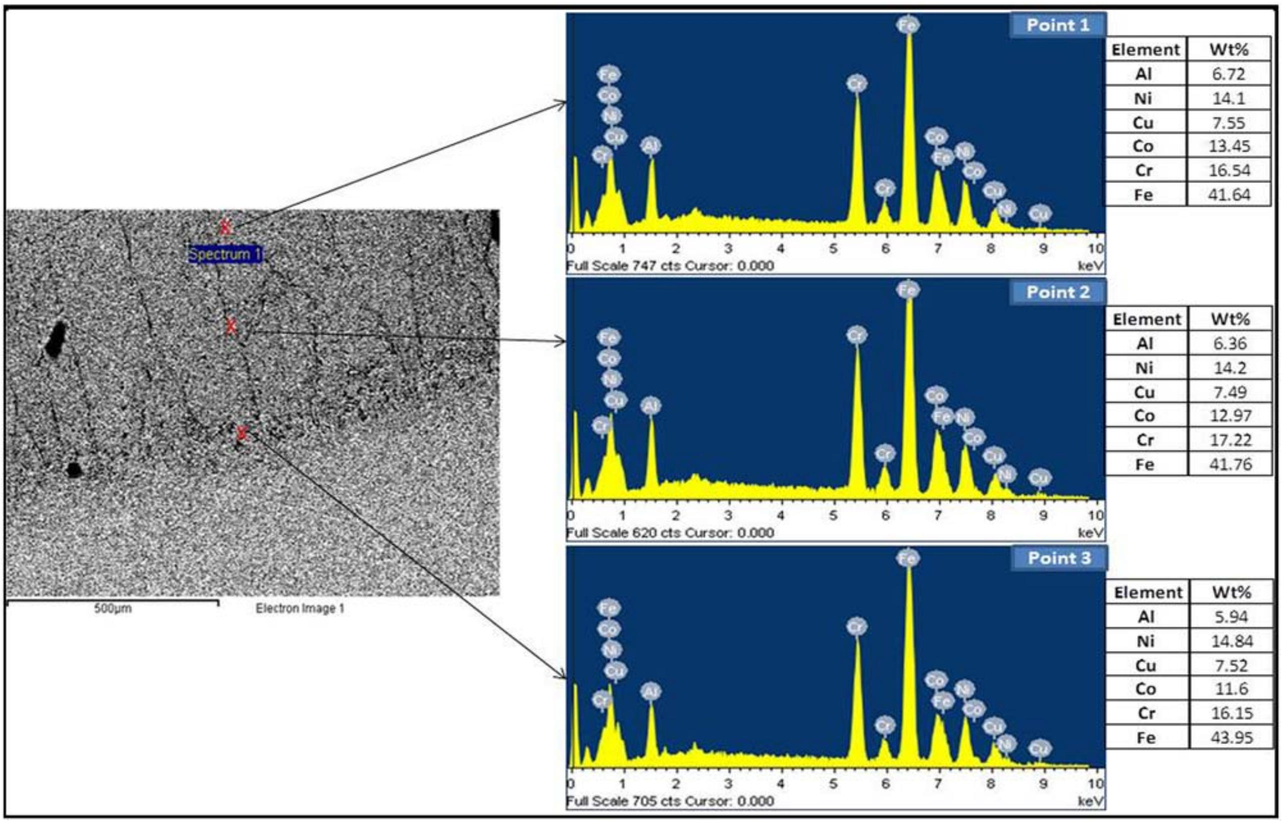

Element	Wt%
Al	6.72
Ni	14.1
Cu	7.55
Co	13.45
Cr	16.54
Fe	41.64

Element	Wt%
Al	6.36
Ni	14.2
Cu	7.49
Co	12.97
Cr	17.22
Fe	41.76

Element	Wt%
Al	5.94
Ni	14.84
Cu	7.52
Co	11.6
Cr	16.15
Fe	43.95

Figure 14: EDS elemental analysis.

Table 9: Magnitude of coefficient of friction

Target material	μ_P	μ_{SS}	$\Delta\mu$
SS-316	0.5948	0.5643	0.0305
Laser cladded SS-316	0.3846	0.3640	0.0206

μ_P, μ_{SS} = peak and steady-state coefficient of friction, $\Delta\mu$ = fluctuation of coefficient of friction.

friction of approximately 0.3846 and 0.5948, respectively. Figure 15 also indicates that the specimen without laser cladding exhibits relatively large fluctuation ($\Delta\mu$ = 0.00305), whereas specimen without laser cladding (SS 316) does show a small fluctuation ($\Delta\mu$ = 0.00206). Primary two reasons cause considerable variation in friction coefficient: (1) periodic localized fracture of the surface layer and (2) periodic aggregation and removal of debris from the worn surface. The friction coefficient was found to increase as the large-sized debris aggregate on the worn surface, while it decreases as the debris eliminate from the worn surface. The coefficient of friction for substrate (SS-316) is larger than that of the HEA cladded SS-316. The coefficient of friction for the sample with laser cladding and without laser cladding varies in between 0.28–0.37 and 0.48–0.57, respectively, as shown in Figure 15.

The reduction in friction coefficient also reduces the shear force at the contact face. As a result, the mass of peeling in a coated surface reduced per unit time. In accordance with the molecular-kinematic and mechanical model theories of the frictional behavior of elastomeric materials, the magnitude of the frictional coefficient is inversely proportional to the hardness of the target surface. The reduction in friction coefficient reduces the shear force at the contact face, which reduces the chances of the occurrence of the adhesive wear. On the other hand, Archard's law indicates that the sliding wear resistance is proportional to the alloy hardness [30,31]. The wear resistivity of SS-316 and HEA cladded SS-316 is shown in Figure 16. The average mass loss of SS-316 (substrate) is 107.8 mg, while the average mass loss of HEA cladded SS-316 is only 64.3 mg. The standard deviations for HEA cladded specimen and substrate SS-316 are 5.62 and 7.89, respectively. This magnitude of mass loss indicates that wear resistivity of SS-316 has been improved by 40.35% after laser cladding of HEA powder.

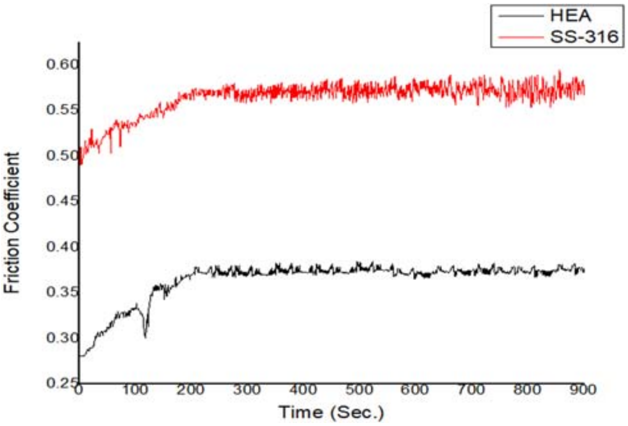

Figure 15: Coefficient of friction for SS-316 and HEA cladded SS-316.

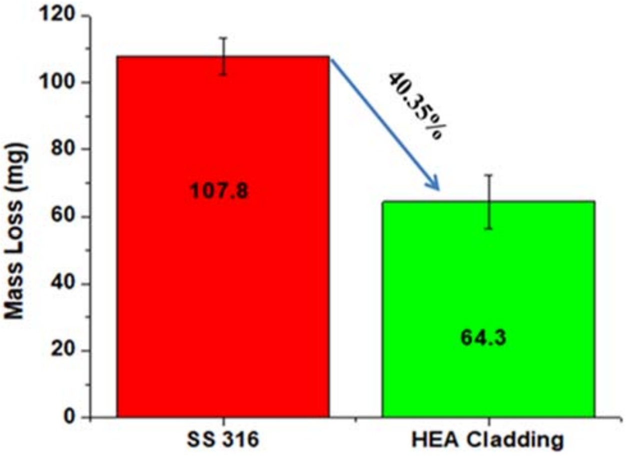

Figure 16: Mass loss comparison.

In order to analyze the wear mechanism of samples with and without laser cladding, the worn surface morphologies of the target material were investigated by SEM (Hitachi-3400) as shown in Figure 17. It was noted that the prominent wear mechanism is abrasive with the indentation of microploughing and plastic deformation. The worn surface of a specimen without laser cladding (substrate) is more severe compared with laser cladded specimen. As shown in Figure 17(c and d), the substrate (SS-316) worn surface consisted of deep grooves with plastic deformation. Furthermore, some wear debris was peeled off from the worn surface. On the other hand, the worn surface of the coated specimen occupied finer grooves as shown in Figure 17(a and b). As compared to the substrate AISI 316, the worn surfaces of the laser cladded specimen shown in Figure 17(a and b) have less peel holes, adhesive zones, ploughed grooves and slighter scaling chips due to the enhancement in hardness. The variation in the hardness and cracking susceptibility leads to convert wear mechanism from micro cutting to delamination wear for substrate to HEA cladded SS-316, respectively. The high microhardness of the coating material leads to enhanced resistivity from the micro cutting [32–35]. As shown in

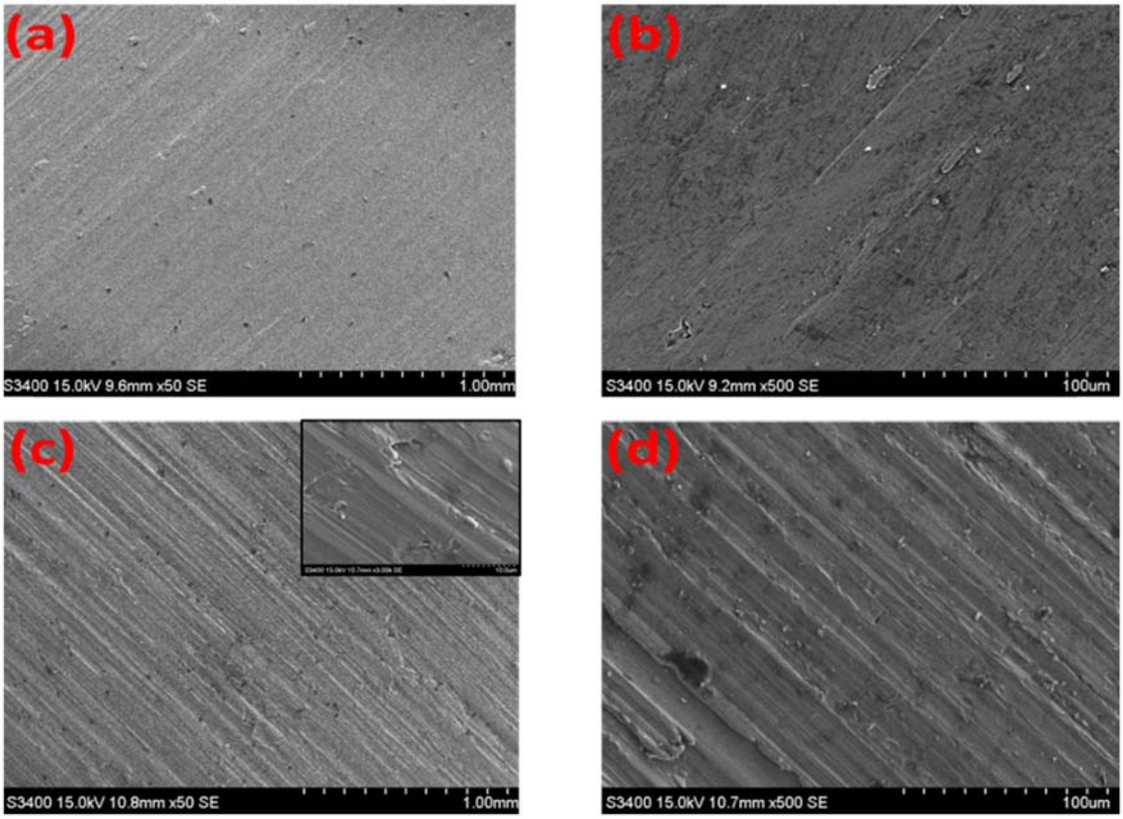

Figure 17: SEM morphologies of worn surfaces for (a and b) HEA cladded SS-316 and (c and d) untreated SS-316.

Figure 17, the mechanism of wear changes to adhesive wear to abrasive wear for substrate (SS-316) and HEA-coated specimens, respectively. The disappearance of adhesive wear was due to not only an increase in microhardness but also the decrease in the friction coefficient.

4 Conclusion

In this research article, multi-response optimization of laser cladding operating parameters was carried out and the wear test was conducted on the multi-track cladding sample achieved through optimum laser cladding process parameters. Based on the above research, the following conclusion can be drawn.

- Clad height and clad width rise with increment in powder feed rate. On the other hand, the clad depth and percentage dilution have inverse relationship with powder feed rate. Clad depth, dilution percentage and clad width decrease with increment in scanning speed. However, the clad height increases.
- ANOVA results for percentage dilution indicate that dilution is significantly influenced by the scanning speed with a contribution of 70.70% and $P = 0.001$, followed by powder feed rate with a contribution of 26.48% and $P = 0.009$.
- The optimum operating parameter combination for maximum cladding height, maximum cladding width, minimum penetration depth and minimum dilution were laser power: 1.1 kW, powder feed rate: 4 g/min and scanning speed: 500 mm/min.
- The XRD results indicate that an increase in the dilution percentage leads to additional peak in terms of iron. The quick directional solidification can be observed at the interface zone of the cladding where the growth direction of the columnar grains is perpendicular to the interface line. It is caused by the high temperature gradient in laser-assisted cladding process. The columnar grains transform to equiaxed grains with reducing temperature gradient in the center of the coatings. The clad coating with minimum dilution (47.8%) is free from pores and cracks, while coating with maximum dilution (71.7%) consists of some interface cracks and pores. The fine cracks at interface for maximum dilution sample were attributed to the high temperature gradient between cladding layer and substrate due to the low powder feed rate and slow scanning speed.

- The microhardness results revealed that the magnitude of microhardness enhances with decrease in percentage dilution. The maximum microhardness (241 HV) was achieved at minimum percentage dilution (47.8%) and clad parameters at 500 mm/min scanning speed and 4 g/min powder feed rate; while at 300 mm/min laser scanning velocity and 2 g/min cladding powder feed rate, the average hardness was 180 HV due to the maximum dilution of 71.7%. The reason behind the decrease in microhardness is due to the influence of the substrate property on the cladding structure. The average microhardness of the coating layer reduced linearly with increase in dilution (20% reduction).
- The multi-track coating was deposited with optimum parameters of single track and subjected to wear testing. It was revealed that the friction coefficient of substrate (SS-316) is larger than that of the HEA cladded SS-316. The wear resistivity of AISI 316 steel has been significantly enhanced after multi-pass laser cladding (60% overlapping ratio) of HEA powder, with optimum laser cladding process parameters determined by multi-response optimization. The wear resistivity of SS-316 has been enhanced by 40.35% after laser-assisted HEA coating.

Funding information: The author appreciates the funding provided by the Department of Science and Technology, India (DST-EMR/2016/000451).

Author contributions: Jyoti Menghani: conceptualization, writing original draft, review and editing; Akash Vyas: conceptualization, conducting experimental work and writing original draft; Satish More: suggestion and implementation about selection of individual principle elements for the high entropy alloy coating; Christ Paul: laser cladding experiment were carried out in his laboratory with valuable guidance for selecting range of process parameters; Amar Patnaik: carried out interpretation of statistical and metallurgical characterization.

Conflicts of interest: The authors declare no conflict of interest.

References

[1] Yeh, J. W., S. Y. Chang, Y. D. Hong, S. K. Chen, and S. J. Lin. Anomalous decrease in X-ray diffraction intensities of Cu–Ni–Al–Co–Cr–Fe–Si alloy systems with multi-principal elements. *Materials Chemistry and Physics*, Vol. 103, No. 1, 2007, pp. 41–46.

[2] Yeh, J. W., S. K. Chen, S. J. Lin, J. Y. Gan, T. S. Chin, T. T. Shun, and S. Y. Chang. Nanostructured high-entropy alloys with multiple principal elements: novel alloy design concepts and outcomes. *Advanced Engineering Materials*, Vol. 6, No. 5, 2004, pp. 299–303.

[3] Zhang, S., C. L. Wu, J. Z. Yi, and C. H. Zhang. Synthesis and characterization of FeCoCrAlCu high-entropy alloy coating by laser surface alloying. *Surface and Coatings Technology*, Vol. 262, 2015, pp. 64–69.

[4] Ye, X., M. Ma, W. Liu, L. Li, M. Zhong, Y. Liu, and Q. Wu. Synthesis and characterization of high-entropy alloy AlXFeCoNiCuCr by laser cladding. *Advances in Materials Science and Engineering*, Vol. 2011, 2011, id. 485942.

[5] Fatoba, O. S., P. A. Popoola, S. L. Pityana, and O. S, Adesina. Computational dynamics of anti-corrosion performance of laser alloyed metallic materials. *Fiber Laser*, 2016, pp. 345–365.

[6] Zhang, H., Y. Pan, Y. He, and H. Jiao. Microstructure and properties of 6FeNiCoSiCrAlTi high-entropy alloy coating prepared by laser cladding. *Applied Surface Science*, Vol. 257, No. 6, 2011, pp. 2259–2263.

[7] Sun, S., Y. Durandet, and M. Brandt. Parametric investigation of pulsed Nd: YAG laser cladding of stellite 6 on stainless steel. *Surface and Coatings Technology*, Vol. 194, No. 2–3, 2005, pp. 225–231.

[8] Hofman, J. T., B. Pathiraj, J. Van Dijk, D. F. De Lange, and J. Meijer. A camera based feedback control strategy for the laser cladding process. *Journal of Materials Processing Technology*, Vol. 212, No. 11, 2012, pp. 2455–2462.

[9] Ansari, M., R. S. Razavi, and M. Barekat. An empirical-statistical model for coaxial laser cladding of NiCrAlY powder on Inconel 738 superalloy. *Optics & Laser Technology*, Vol. 86, 2016, pp. 136–144.

[10] Goodarzi, D. M., J. Pekkarinen, and A. Salminen. Effect of process parameters in laser cladding on substrate melted areas and the substrate melted shape. *Journal of Laser Application*, Vol. 27, No. S2, 2015, id. S29201.

[11] Zhang, H., Y. Shi, M. Kutsuna, and G. J. Xu. Laser cladding of Colmonoy 6 powder on AISI316L austenitic stainless steel. *Nuclear Engineering and Design*, Vol. 240, No. 10, 2010, pp. 2691–2696.

[12] Zhao, Y., F. Zhou, J. Yao, S. Dong, and N. Li. Erosion–corrosion behavior and corrosion resistance of AISI 316 stainless steel in flow jet impingement. *Wear*, Vol. 328, 2015, pp. 464–474.

[13] Boer, F. D., R. Boom, W. C. M. Mattens, A. R. Miedema, and A. K. Niessen. “Cohesion in metals: transition metal alloys,” *FR* de Boer *and* DG Pettifor (*series eds.*), Vol. 1, 1988.

[14] Zhang, S., C. L. Wu, and C. H. Zhang. Phase evolution characteristics of FeCoCrAlCuVxNi high entropy alloy coatings by laser high-entropy alloying. *Materials Letters*, Vol. 141, 2015, pp. 7–9.

[15] Kattire, P., S. Paul, R. Singh, and W. Yan. Experimental characterization of laser cladding of CPM 9V on H13 tool steel for die repair applications. *Journal of Manufacturing Processes*, Vol. 20, 2015, pp. 492–499.

[16] Zhang, H., Y. Shi, M. Kutsuna, and G. J. Xu. Laser cladding of Colmonoy 6 powder on AISI316L austenitic stainless steel. *Nuclear Engineering and Design*, Vol. 240, No. 10, 2010, pp. 2691–2696.

[17] Sun, Y., and M. Hao. Statistical analysis and optimization of process parameters in Ti6Al4V laser cladding using Nd: YAG laser. *Optics and Lasers in Engineering*, Vol. 50, No. 7, 2012, pp. 985–995.

[18] Maruda, R. W., G. M. Krolczyk, E. Feldshtein, P. Nieslony, B. Tyliszczak, and F. Pusavec. Tool wear characterizations in finish turning of AISI 1045 carbon steel for MQCL conditions. *Wear*, Vol. 372, 2017, pp. 54–67.

[19] Wu, C. L., S. Zhang, C. H. Zhang, H. Zhang, and S. Y. Dong. Phase evolution and cavitation erosion-corrosion behavior of FeCoCrAlNiTix high entropy alloy coatings on 304 stainless steel by laser surface alloying. *Journal of Alloys and Compounds*, Vol. 698, 2017, pp. 761–770.

[20] Gao, Y. L., M. Jie, and H. B. Zhang. Influence of laser scanning speed on Cu–Zr–Al composite coatings on Mg alloys. *International Journal of Minerals, Metallurgy, and Materials*, Vol. 20, No. 6, 2013, pp. 568–573.

[21] Desale, G. R., C. P. Paul, B. K. Gandhi, and S. C. Jain. Erosion wear behavior of laser clad surfaces of low carbon austenitic steel. *Wear*, Vol. 266, No. 9–10, 2009, pp. 975–987.

[22] Zhang, Y., Y. J. Zhou, J. P. Lin, G. L. Chen, and P. K. Liaw. Solid-solution phase formation rules for multi-component alloys. *Advanced Engineering Materials*, Vol. 10, No. 6, 2008, pp. 534–538.

[23] Sheng, G. U. O., and C. T. Liu. Phase stability in high entropy alloys: formation of solid-solution phase or amorphous phase. *Progress in Natural Science: Materials International*, Vol. 21, No. 6, 2011, pp. 433–446.

[24] Fang, S., X. Xiao, L. Xia, W. Li, and Y. Dong. Relationship between the widths of super cooled liquid regions and bond parameters of Mg-based bulk metallic glasses. *Journal of Non-Crystalline Solids*, Vol. 321, No. 1–2, 2003, pp. 120–125.

[25] Takeuchi, A., and A. Inoue. Classification of bulk metallic glasses by atomic size difference, heat of mixing and period of constituent elements and its application to characterization of the main alloying element. *Materials Transactions*, Vol. 46, No. 12, 2005, pp. 2817–2829.

[26] Massalski, T. B. Comments concerning some features of phase diagrams and phase transformations. *Materials Transactions*, Vol. 51, No. 4, 2010, pp. 583–596.

[27] Zhang, S., C. L. Wu, J. Z. Yi, and C. H. Zhang. Synthesis and characterization of FeCoCrAlCu high-entropy alloy coating by laser surface alloying. *Surface and Coatings Technology*, Vol. 262, 2015, pp. 64–69.

[28] Qiu, X. W., Y. P. Zhang, and C. G. Liu. Effect of Ti content on structure and properties of Al2CrFeNiCoCuTix high-entropy alloy coatings. *Journal of Alloys and Compounds*, Vol. 585, 2014, pp. 282–286.

[29] Shang, C., E. Axinte, W. Ge, Z. Zhang, and Y. Wang. High-entropy alloy coatings with excellent mechanical, corrosion resistance and magnetic properties prepared by mechanical alloying and hot pressing sintering. *Surfaces and Interfaces*, Vol. 9, 2017, pp. 36–43.

[30] Wu, J. M., S. J. Lin, J. W. Yeh, S. K. Chen, Y. S. Huang, and H. C. Chen. Adhesive wear behavior of AlxCoCrCuFeNi high-entropy alloys as a function of aluminum content. *Wear*, Vol. 261, No. 5–6, 2006, pp. 513–519.

[31] Zhang, P., H. Yan, P. Xu, Z. Yu, and C. Li. Microstructure and tribological behavior of amorphous and crystalline composite coatings using laser melting. *Applied Surface Science*, Vol. 258, No. 18, 2012, pp. 6902–6908.

[32] Wang, Y., Y. Yang, H. Yang, M. Zhang, S. Ma, and J. Qiao. Microstructure and wear properties of nitride AlCoCrFeNi high-entropy alloy. *Materials Chemistry and Physics*, Vol. 210, 2018, pp. 233–239.

[33] Li, G. J., J. Li, and X. Luo. Effects of high temperature treatment on microstructure and mechanical properties of laser-clad NiCrBSi/WC coatings on titanium alloy substrate. *Materials Characterization*, Vol. 98, 2014, pp. 83–92.

[34] Zhang, P., H. Yan, C. Yao, Z. Li, Z. Yu, and P. Xu. Synthesis of Fe–Ni–B–Si–Nb amorphous and crystalline composite coatings by laser cladding and remelting. *Surface and Coatings Technology*, Vol. 206, No. 6, 2011, pp. 1229–1236.

[35] Weng, F., H. Yu, C. Chen, J. Liu, L. Zhao, J. Dai, and Z. Zhao. Effect of process parameters on the microstructure evolution and wear property of the laser cladding coatings on Ti–6Al–4V alloy. *Journal of Alloys and Compounds*, Vol. 692, 2017, pp. 989–996.